

Analyst

Accepted Manuscript



This is an *Accepted Manuscript*, which has been through the Royal Society of Chemistry peer review process and has been accepted for publication.

Accepted Manuscripts are published online shortly after acceptance, before technical editing, formatting and proof reading. Using this free service, authors can make their results available to the community, in citable form, before we publish the edited article. We will replace this *Accepted Manuscript* with the edited and formatted *Advance Article* as soon as it is available.

You can find more information about *Accepted Manuscripts* in the [Information for Authors](#).

Please note that technical editing may introduce minor changes to the text and/or graphics, which may alter content. The journal's standard [Terms & Conditions](#) and the [Ethical guidelines](#) still apply. In no event shall the Royal Society of Chemistry be held responsible for any errors or omissions in this *Accepted Manuscript* or any consequences arising from the use of any information it contains.

1
2
3 **High resolution mass spectrometry imaging of plant tissues: towards a plant metabolite**
4 **atlas**
5

6 Dhaka Ram Bhandari¹, Qing Wang², Wolfgang Friedt², Bernhard Spengler¹, Sven
7 Gottwald^{2*}, Andreas Römpf^{1*}
8
9

10 ¹Justus Liebig University Giessen, Institute of Inorganic and Analytical Chemistry,
11 Schubertstrasse 60, building 16, 35392 Giessen, Germany; ²Justus Liebig University Giessen,
12 Department of Plant Breeding, IFZ, Justus Liebig University Giessen, Heinrich-Buff-Ring 26-
13 32, 35392 Giessen, Germany
14
15
16
17
18
19

20
21 *Author for correspondence:

22 *Sven Gottwald*

23 *Tel: +49641-9937426*

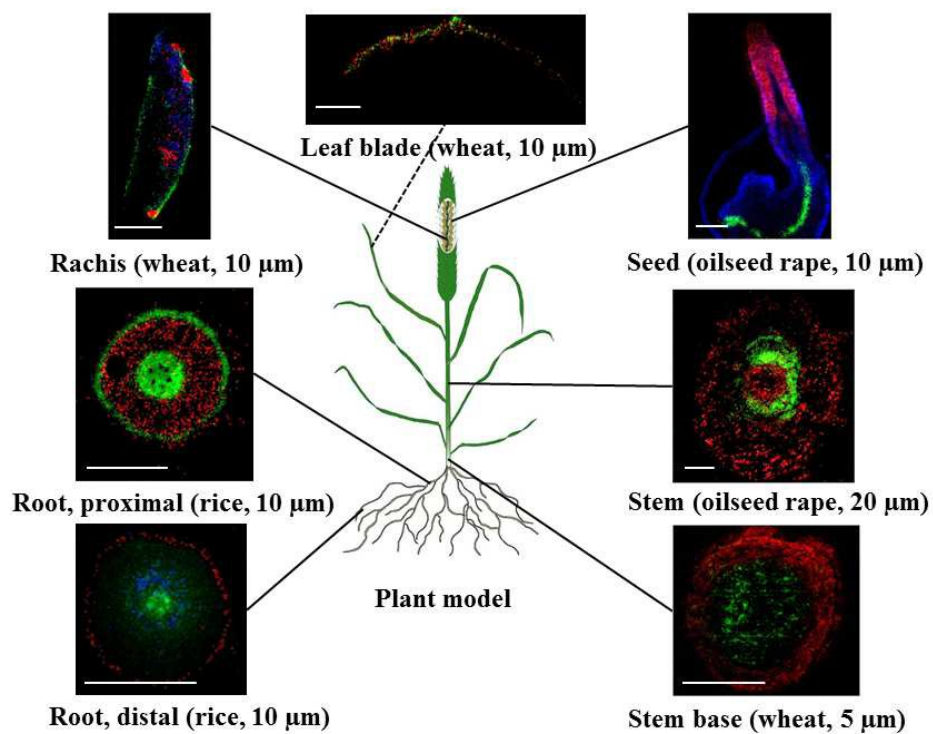
24 *Sven.Gottwald@agrar.uni-giessen.de*
25
26
27

28
29 *Andreas Römpf*

30 *Tel: +49641-9934802*

31 *Andreas.Roempf@anorg.Chemie.uni-giessen.de*
32
33
34
35
36
37
38
39
40
41
42
43
44
45
46
47
48
49
50
51
52
53
54
55
56
57
58
59
60

Graphical Abstract



Label-free chemical imaging of a wide range of metabolites in all major plant organs acquired at high spatial resolution.

Summary

Mass spectrometry (MS) imaging provides spatial and molecular information for a wide range of compounds. This tool can be used to investigate metabolic changes in plant physiology and environmental interaction. A major challenge in our study was to prepare tissue sections that were compatible with high spatial resolution analysis and therefore dedicated sample preparation protocols were established and optimized for the physicochemical properties of all major plant organs. We combined high spatial resolution (5 μ m), in order to detect cellular features, and high mass accuracy (< 2 ppm root mean square error), for molecular specificity. Mass spectrometry imaging experiments were performed in positive and negative mode. Changes in metabolite patterns during plant development were investigated for germination of oilseed rape. The detailed localization of more than 90 compounds allowed assignments to metabolic processes and indicated possible functions in plant tissues. The ‘untargeted’ nature of MS imaging allows the detection of marker compounds for the physiological status, as demonstrated for plant-pathogen interaction. Our images show excellent correlation with optical/histological examination. In contrast to previous MS imaging studies of plants, we present a complete workflow that covers multiple species, such as oilseed rape, wheat seed and rice. In addition, different major plant organs and a wide variety of compound classes were analyzed. Thus, our method could be used to develop a plant metabolite atlas as a reference to investigate systemic and local effects of pathogen infection or environmental stress.

Key words: *Fusarium graminearum*, high mass resolution, high spatial resolution, mass spectrometry imaging, metabolites, oilseed rape, wheat

1 **1 Introduction**

2 Plants are major suppliers of food and natural resources used in pharmaceuticals, cosmetics,
3 and fine chemicals. As sessile organisms, plants cannot escape their environment, instead
4 (progressive) acclimatization by specific metabolic adjustments is the only response to
5 changing conditions ¹. This resulted in a complex metabolism with over 200,000 known
6 primary and secondary metabolites ².

7 As part of the 'omics' field, metabolic studies have been applied to a wide spectrum of topics
8 in plant science. These include basic research in model plants such as *Arabidopsis* to discover
9 fundamental biosynthetic processes and metabolic networks ³ as well as applied research in
10 crop plants such as wheat (*Triticum aestivum*) and oilseed rape (*Brassica napus*) to uncover
11 biochemical mechanisms behind complex agronomical traits and phenotypes ⁴. Important
12 current issues in crop plant research are developmental plasticity ⁵, responses to abiotic ⁶ and
13 biotic stress ⁷. In contrast to genes, metabolites are the end products of cellular processes and
14 therefore, can serve as direct signatures of biochemical activity ⁸. Metabolomics studies are
15 typically based on mass spectrometry (MS), hyphenated with techniques such as gas and
16 liquid chromatography, covering an extensive variety of compound classes and concentration
17 ranges. In these studies, usually homogenized samples are used, resulting in a loss of spatial
18 information. On the other hand, visualization has become an important topic in plant science,
19 because detailed knowledge on metabolite distributions in plants is fundamental for the
20 understanding of local regulatory networks, which underlay selected traits ⁹. Visualization is
21 usually achieved by fluorescence microscopy, *in situ* hybridization or immunohistochemistry
22 ¹⁰, techniques which provide high spatial resolution, but chemical information is typically
23 limited to very few compounds per experiment.

24 Mass spectrometry (MS) imaging combines spatial information and molecular information for
25 a wide range of compounds. This method can, therefore, complement the classical approaches
26 of metabolomics studies and microscopic methods. MS imaging is the method of scanning a
27 sample of interest and generating images of the intensity distribution of analyte ions. In
28 contrast to classical histochemical methods, MS imaging is a label free technique and thus,
29 can be used without prior knowledge of the analyte. Due to this untargeted nature, hundreds
30 of compounds can be detected simultaneously. While numerous studies are published in the
31 field of clinical research, plant research is a relatively new application of MS imaging which,

1
2
3 32 however, offers important advantages for the detailed investigation of metabolites from
4 33 complex plant tissues ^{7, 11}.

5
6 34 The first studies using MALDI imaging on plants analyzed the distribution of agrochemical
7 35 compounds in soya bean (*Glycine max*) ¹² and carbohydrates in wheat (*Triticum aestivum*)
8 36 stem ¹³. Subsequent studies included applications on rice (*Oryza sativa*) seeds ^{14, 15}, flowers
9 37 and roots of the model plant *Arabidopsis thaliana* ¹⁶⁻¹⁹ and barley (*Hordeum vulgare*) seeds ²⁰.
10 38 However, most MS imaging studies in plants were performed with MALDI-TOF instruments,
11 39 which provide lower mass resolution data, possibly leading to ambiguous results. Only
12 40 recently, high mass resolution orbital trapping mass analyzers were applied ^{16, 21-24}. A pixel
13 41 size of 25 μm ^{25, 26} and 5 μm ²⁷ was obtained in selected experiments, but most studies were
14 42 performed at 100 to 200 μm spatial resolution. A related method is laser desorption ionization
15 43 (LDI) which was used for the analysis of plant tissue with a TOF mass spectrometer at 10 μm
16 44 pixel size.²⁸ This approach does not require any matrix application, but is limited to
17 45 compounds with UV-absorbing functional groups.

18 46 We have introduced a MS imaging method that combines for the first time high selectivity (1
19 47 ppm mass accuracy) and high spatial resolution (3 to 10 μm pixel size) in one experiment ²⁹.
20 48 This results in a significantly improved reliability of compound identifications and provides
21 49 molecular information on a cellular level. This technique was initially developed for
22 50 mammalian tissues ³⁰, but has now been further developed and optimized for non-mammalian
23 51 tissues. Recently, we have demonstrated the applicability of MS imaging for metabolite
24 52 characterizations of wine (*Vitis vinifera*) grapes ³¹, the bird's nest fungus *Cyathus striatus* ³²
25 53 and the licorice (*Glycyrrhiza glabra*) rhizome ³³ at 20 μm , 15 μm and 10 μm pixel size,
26 54 respectively.

27 55 Previous MS imaging studies of plants were limited to a selected organ in a particular species
28 56 and typically focused on a certain compound class. In this publication we present new
29 57 developments in MS imaging of plant tissues that enable a comprehensive investigation of the
30 58 plant metabolome. These developments include the first MS imaging experiments at 5 μm
31 59 pixel size which reveal the detailed structure of metabolites in plant organs. We were able to
32 60 image a wide range of compound classes including different phenolic compounds,
33 61 phospholipids and other lipid species, carbohydrates, phenolic choline esters, glycosides, and
34 62 glycerides in mature and germinating oilseed rape. These data probably represent the most
35 63 comprehensive spatially resolved information about metabolites in plants, so far.

36 64 To establish a plant metabolome atlas, it is necessary to analyze all relevant plant organs and
37 65 to cover different plant species. This primarily concerns the development of dedicated sample

1
2
3 66 preparation techniques. In plants, different organs and tissues are specialized and modified for
4 67 specific functions. Thus sample preparation techniques need to be adapted to the different
5
6 68 plant organs and (metabolic) stages. Consequently, we also present developments in MS
7
8 69 imaging, which concern sectioning procedures that were optimized for high spatial resolution
9
10 70 analysis in a variety of tissues with specific physicochemical properties.

11 71 The methodological approach and obtained information of MS imaging is discussed in detail
12
13 72 in a case study comparing mature and germinating seed of oilseed rape (section 2.1).
14
15 73 Subsequently additional plant species and organs are discussed. This includes experiments in
16
17 74 negative ion mode and with 5 μm pixel size for wheat seed (2.2). Sample preparation is the
18
19 75 focus for wheat rachis (2.3), wheat stem base (2.4) and rice root (2.5). Finally, we show an
20
21 76 example in which a wheat seed infected by the fungal pathogen *Fusarium graminearum* is
22
23 77 compared to an uninfected seed and cultured fungal mycelium (2.6). Details of the
24
25 78 experimental procedure for each experiment in particular sample preparation are discussed in
26
27 79 Experimental section (3.).

28 80 In the Conclusions section (4.) we have included measurements of additional plant organs
29
30 81 (distal root, leaf and stem). We also discuss the idea of how our MS imaging approach could
31
32 82 be used to build up an atlas of the plant metabolome as a reference to detect systemic and
33
34 83 local metabolic changes.
35
36 84
37 85
38 86

1
2
3
4
5
6
7
8
9
10
11
12
13
14
15
16
17
18
19
20
21
22
23
24
25
26
27
28
29
30
31
32
33
34
35
36
37
38
39
40
41
42
43
44
45
46
47
48
49
50
51
52
53
54
55
56
57
58
59
60

87 2 Results and Discussion

88 2.1 Mapping of metabolic processes in seed development

89 Maturity and germination are metabolically highly active stages during the development with
90 significant implications for subsequent plant performance^{35, 36} and nutritional quality of seed
91 products³⁷. Therefore, these stages were chosen to establish high resolution MS imaging as a
92 tool for mapping metabolites.

93 Seeds of oilseed rape are 2-3 mm in diameter, which makes direct cryosectioning challenging.
94 Therefore, cellulose (CMC) solution was used as an embedding material as described in the
95 experimental section. The optical image of both the stages (Fig. 1a and 1b) can be directly
96 correlated to the respective ion images (Fig 1c, 1e, 1d 1f). A mass spectrum acquired from a
97 single 10 μm pixel in the shoot apical meristem region of germinating seed is shown in Fig.
98 1g. The exact location of this pixel and the zoomed-in mass spectrum are provided in
99 Supporting Information, Fig. S1. Additional single 10 μm spectra from cotyledon vasculature,
100 nucellar tissue (putative), seed coat, and emerging radicle are shown in the Supporting
101 Information, Fig. S2-S5. Several compounds such as sinapine, methyl sinapate, cyclic
102 spermidine conjugate, triacylglycerols and phosphatidylcholines were detected. These
103 compounds were identified based on accurate mass measurements. For example, sinapine
104 (choline ester of sinapic acid) was detected with a mass error of -0.83 ppm (Fig. 1g) and the
105 corresponding image is shown in Fig. 1c (blue). The root mean square error (RMSE),
106 calculated from 52523 spectra over the full image, was 1.0 ppm. The mass accuracy was
107 better than 2 ppm for all compounds assigned in this article. This demonstrated a reliable
108 detection of compounds also under imaging conditions. Using high resolution and high mass
109 accuracy, it is possible to generate MS images with a narrow bin width of $\Delta m/z = \pm 5$ ppm,
110 thus preventing interference from neighboring peaks (an example is discussed for the MS
111 imaging on wheat seed). This bin width was used for all MS images presented in this study. A
112 list of 93 compounds imaged in oilseed rape (including mass accuracy values) is given in
113 Supporting Information, Table S1, and the respective MS images are compiled in Supporting
114 Information, Fig. S6 (germination) and Fig. S7 (maturation). The sequential numbering of
115 compounds in Table S1 corresponds to the index numbers in Fig. S6 and Fig. S7. For
116 example, the MS images of sinapine (compound No. 1) are shown in Fig. S6.1 and Fig. S7.1.
117 These images are selected ion images of a single compound (allowing visualization of pixels
118 with lower signal intensities), in contrast to the combined RGB images in Fig. 1.

1
2
3 119 The compound identification can be further assisted by on-tissue MS/MS experiments as
4 120 demonstrated for sinapine in Fig. 1h, showing the single pixel on-tissue tandem mass
5 121 spectrum. The fragment ion at m/z 251 corresponds to a loss of trimethylamine from the
6 122 choline group. Additional fragment ions can be attributed to sequential loss of C_2H_4O (m/z
7 123 207), CH_3OH (m/z 175) and CO (m/z 147). All fragment ions were detected with a mass error
8 124 of less than 1 ppm. This fragmentation pattern is also in accordance with electrospray-based
9 125 MS/MS data ³⁸, thus confirming the initial identification which was based on accurate mass
10 126 data.

11 127 In the mature seed, sinapine was distributed throughout the entire embryo (Fig. 1d, blue)
12 128 which consists of the cotyledons and the hypocotyl-radicle region (Fig. 1b). This broad
13 129 distribution of sinapine was found to persist during the early germination (Figure 1c, blue). In
14 130 contrast, cyclic spermidine conjugate showed a distinct distribution in the hypocotyl-radicle
15 131 region in the mature seed (Fig. 1d, red, appears magenta due to overlay with sinapine in blue),
16 132 and in the germinating seed their activities shifted to the emerging radicle (Fig. 1c, red). This
17 133 demonstrates that MS imaging is able to detect shifts in metabolite distribution at different
18 134 developmental stages. Since a second spermidine conjugate, the N1,N5,N10-tricaffeoyl
19 135 spermidine, showed a similar spatial distribution (Fig. 1e and 1f red), our results suggest that
20 136 spermidine conjugates play a role in the development of the hypocotyl-radicle, which later
21 137 differentiates into the plant root and stem (a more detailed discussion is given in Supporting
22 138 Information, Notes S1).

23 139 The distribution of the compounds mentioned above corresponds very well to the hitherto
24 140 only tissue-specific metabolite mapping in oilseed rape, carried out by combining laser
25 141 microdissection and HPLC-DAD/MS ³⁹. This demonstrates both the ability of MS imaging to
26 142 confirm findings from alternative techniques and significantly improve details on spatial
27 143 distributions. The approach applied by Fang et al. ³⁹ allowed differentiating between inner and
28 144 outer cotyledon in the mature seed. MS imaging at high spatial resolution, however, enabled
29 145 to allocate metabolites to more detailed morphological features. For instance, sinapoyl
30 146 glucose, previously identified in a bulk analysis of oilseed rape ⁴⁰, was mapped at both seed
31 147 developmental stages to a thin layer between the two cotyledons (Fig. 1c, d, green). This
32 148 region corresponds to the adaxial (upper) cotyledon epidermis which also contained different
33 149 kaempferol derivatives (Fig. S6.30-6.33; Fig. S71.30-7.33). Therefore, these compounds might
34 150 contribute to the epidermal shield against various abiotic stress factors such as UV-B
35 151 radiation ^{41, 42}. In contrast, the choline ester 'UC#1' was mapped at both seed stages in the
36 152 outer layer of cotyledons, representing the abaxial (lower) cotyledon epidermis (Fig. 1e, f,

1
2
3 153 blue). UC#1 belongs to a group of 'unknown' choline esters which were initially detected in
4 154 mature oilseed rape^{43, 44}. The possibility to map compounds even in the epidermis layers,
5
6 155 makes MS imaging an interesting tool to examine metabolomic processes.

7
8 156 Feruloylcholine guaiacyl (FC(4-O-8')G) was distributed throughout the mature embryo (Fig.
9
10 157 1f, green), but demonstrated different and more specific accumulations in the germinating
11 158 embryo, i.e. in the parenchyma layer of emerging hypocotyl and shoot apical meristem (Fig.
12
13 159 1e, green). The general presence of feruloylcholine FC(4-O-8')-guaiacyl in oilseed rape has
14
15 160 previously been reported⁴³.

16
17 161 MS imaging is a direct analysis, which does not require preliminary extraction to detect a
18
19 162 wide range of compound classes from a single tissue section. In fact, the obtained results were
20
21 163 in agreement with other untargeted hyphenated-MS techniques which used extraction of the
22
23 164 whole seed^{43, 44} or more specific analysis including laser microdissection and HPLC-
24
25 165 DAD/MS³⁹. The high-resolution images generated by our MS imaging method provide much
26
27 166 more detailed spatial distributions, which enable elucidation of biological metabolite
28
29 167 functions.

30
31 168 This data can be used to investigate metabolomic networks. An example is the sinapate ester
32
33 169 metabolism presented in Fig. 2, Fig. S8 and Fig. S9, which is relevant for oil production⁴⁶. In
34
35 170 this pathway not only abundant metabolites such as sinapine, coumaric acid and kaempferol
36
37 171 compounds were mapped, but also less abundant compounds such as methyl sinapate with
38
39 172 unknown functions. So far, methyl sinapate has rarely been reported^{43, 47}. MS imaging has
40
41 173 located this compound in the entire mature embryo as well as in the outer cotyledon,
42
43 174 hypocotyl and radicle in the germinating stage (Fig. 2). Since the biological function of
44
45 175 methyl sinapate is still unknown, it was interesting to find them remarkably enriched in the
46
47 176 central apical shoot meristem (Fig. 2), indicating a possible function in the developing
48
49 177 hypocotyl. More details on sinapine esters and kaempferol glycosides are shown in
50
51 178 Supporting Information, Notes S2.

52
53
54
55
56
57
58
59
60

180 2.2 Wheat seed

181
182 181 Wheat seed at the soft dough stage of maturity are physiologically mature, but still
183
184 182 characterized by rapid accumulations of starch and nutrients⁴⁸. In contrast to oilseed rape,
185
186 183 wheat seed (dough stage) have higher moisture content (about 40%), but are still elastic
187
188 184 compared to the later stages, such as the postharvest state, which has been analyzed for
189
190 185 oilseed rape. The size and the shape of the wheat seed allowed direct mounting in the

1
2
3 186 cryomicrotome without embedding. This allows tissue section preparation by direct
4 187 cryosectioning. The optical image (Fig. 3a) from a transverse section of germ-region
5 188 (embryo) can be directly correlated to MS images (Fig. 3b). In addition to sample preparation,
6 189 spatial resolution and mass resolution are central parameters for generating high-quality
7 190 images in untargeted metabolite screening. An important reason is the lack of
8 191 chromatographic separation, which makes analyte assignments in MS imaging more
9 192 complicated compared to metabolomic analysis based on GC/MS or LC/MS¹⁶. We combined
10 193 high mass resolution (which allows generating images with a narrow m/z bin width of ± 5
11 194 ppm) with high spatial resolution (5 μm pixel size). This enabled to represent the grain
12 195 architecture with a reliable assignment of imaged metabolites to their respective *in-situ*
13 196 locations. For example, it was possible to demonstrate the specific location of a polyphenol
14 197 glycoside in the protection sheath coleoptile/coleorhizae (Fig. 3b, green), suggesting a
15 198 function in protecting the emerging shoot, plumules and/or radicle against UV-B radiation,
16 199 pathogens or herbivores⁴⁹. In addition, a phosphatidylcholine PC(36:4) was specifically
17 200 located in the scutellum (Fig. 3b, blue), while a phosphatidylglycerol PG(38:2) was restricted
18 201 to the pericarp-seed coat region (Fig. 3b, red). PG membrane lipids are vital for normal
19 202 embryo development as they are involved to form chloroplast thylakoid membranes, which
20 203 are the primary site of photosynthesis⁵⁰. By contrast, high mass resolution (± 5 ppm)
21 204 combined with low spatial resolution results in a loss of spatial information (Fig. 3c), which
22 205 shows the same measurement with a recalculated pixel size of 50 μm . A critical loss of
23 206 information is also observed using a bin width of 0.1, as typically used for MALDI-TOF
24 207 imaging experiments. Here, low mass resolution affects the image generation due to the
25 208 interference of neighboring peaks (Fig. 3d). Consequently, a combination of high mass
26 209 resolution with high spatial resolution is needed to resolve the complexity of metabolites in
27 210 plant tissue sections.

28
29
30
31
32
33
34
35
36
37
38
39
40
41
42
43
44
45
46
47
48
49
50
51
52
53
54
55
56
57
58
59
60
211 Negative ion mode measurements provide a possibility to obtain complementary information
212 on identification of the compounds. A section of the wheat germ similar to Fig. 3a was
213 scanned in negative ion mode (Fig. 4a). For example, the polyphenol glycoside in Fig. 3b
214 (green) was confirmed by having the same spatial distribution in negative ion mode (Fig. 4b,
215 green). Similar distribution of additional polyphenol glycosides is demonstrated by comparing
216 positive and negative ion measurements (Fig. S10). Moreover, the negative mode experiment
217 enables imaging of additional compound classes such as a phosphatidylinositol [PI(34:2)-H]
218 located in the scutellum and endosperm of wheat seed (Fig. 4b, red). PI is a key membrane

1
2
3 219 constituent and an important participant in signaling processes in seed and vegetative tissue⁵¹,
4 220 ⁵², responsible for normal plant growth, stress response and seed germination^{53 54}.

221 **2.3 Wheat spike rachis**

222 The rachis is the primary axis of a cereal spike, which bears the spikelets containing the
223 flowers. The spike rachis consists of low-density tissues, resulting in floating of the specimen
224 in CMC solution (used for oilseed rape, Fig. 1). Therefore, an alternative embedding material,
225 a paste of 15 % (w/v) tragacanth gum in water was employed⁵⁵. The rachis is responsible for
226 the translocation of assimilates into florets and developing seeds⁵⁶, but also the passage for
227 systemic inflorescence colonization by fungal pathogens such as *Fusarium graminearum* in
228 wheat⁵⁷ or *Aspergillus flavus* in maize⁵⁸. Although recent studies have demonstrated the
229 potential of the rachis as an effective defense structure, the molecular and cellular processes
230 behind these defenses are still unknown^{58,59}. The optical image of a transverse rachis section
231 (Fig. 5a) correlates well with the MS image. The MS image shows a polyphenol glycoside
232 located in the epidermis (Fig. 5b, green) and two further metabolites, a
233 lysophosphatidylcholine (Fig. 5b, blue) and a pheophytin (Fig. 5b, red), spatially distributed
234 in the parenchyma cells, which include the photosynthetically active chlorenchyma. In fact,
235 pheophytin is a chlorophyll derivative involved in the electron transfer pathway of
236 photosystem II⁶⁰. In addition to the above mentioned nutritional aspects, compounds such as
237 lysophosphatidylcholine are essentially involved in plant health by functioning in the
238 synthesis of phyto-oxylipins which comprise, for example, antifungal peptides and defense-
239 signaling molecules⁶¹.

240

241 **2.4 Wheat stem base**

242 As the gateway from below- to above-ground plant parts, the stem base is a neuralgic point
243 for the spread of soil-borne pathogens into the upper plant organs⁶². The stem base of wheat
244 seedlings has a relatively high water content compared to seed or rachis. Thus, a faster
245 freezing method was obtained by using a coolant mixture of dry ice and hexane. The diameter
246 of a stem base is relatively small for a low spatial resolution measurement. Therefore, a 5 μm
247 step size was selected for MS imaging. As examples, the optical image (Fig. 6a) is well
248 correlated with the ion image, where a polyphenol glycoside was mapped specifically to the
249 leaf sheath (Fig. 6b, red), while a phospholipid was enriched in the stem tissue (Fig. 6b,
250 green). Similarly to the lysophosphatidylcholine reported from the rachis,
251 phosphatidylcholines are involved in the synthesis of phyto-oxylipins such as jasmonates⁶¹

1
2
3 252 which are currently discussed as essential signaling molecules in wheat defences against *F.*
4 253 *graminearum*⁶³. Changes in these phospholipids occur at the site of fungal infection, since
5
6 254 they are rapidly formed in response to pathogen attacks, which makes them useful markers for
7
8 255 induced resistance⁶⁴. Thereby, spatial distributions in diseased tissues could facilitate the
9
10 256 identification of resistance-related lipids.
11
12

13
14
15
16
17
18
19
20
21
22
23
24
25
26
27
28
29
30
31
32
33
34
35
36
37
38
39

258 2.5 Plant roots

259 Roots remained largely unexplored for quite a long time⁶⁵. The soil micro-flora living
260 directly at the surface or within roots facilitates pathogenic interactions and cooperative
261 interactions. The latter improve nutrient uptake, stress resistance and yield performance⁶⁷.
262 Root development and physiology are highly flexible in changing environments. However,
263 the chemical signaling behind these changes, as well as behind the root-microbe interactions
264 is largely unknown⁶⁸.

265 With this background, roots represent an important target for an MS imaging application.
266 First studies towards a procedure that meets the specific requirements of roots, have been
267 conducted on *in vitro*-grown roots of wheat, barley and rice. Cereals have a fibrous system of
268 thin seminal roots with a typically high water content and fragile structure, characteristics that
269 challenge the preparation of tissue sections. The CMC embedding and sectioning in a
270 cryomicrotome as described for aerial plant parts was not successful for root tissue. The large
271 vacuole in the root cell caused the cells to rupture due to the change in temperature (during
272 thawing process). Thin and uniform root cross sections were only obtainable with a common
273 shaving blade.

274 Seminal root tissues were found to be generally very fragile, and the structure integrity was
275 easily lost. While rice root sections were on average 0.8 mm in diameter, wheat and barley
276 root sections were not more than 0.5 mm in diameter. In case of rice roots, it was possible to
277 generate cross sections that were appropriate for MS imaging measurements (Fig. 7a), for
278 wheat and barley the limiting factor was a high fragility together with a low diameter, which,
279 so far, hampers the preparation of cross sections with sufficient quality. Consequently, the MS
280 imaging measurements resulted in low quality ion images, which were not suitable for fine-
281 scale metabolite localization. However, we were able to image a cross section from the
282 elongation zone of seminal rice roots, which had a diameter (ca. 500 μm) similar to wheat and
283 barley roots (Fig. S11). This is most likely related to the fact that root cells in this zone are in

1
2
3 284 the state of elongation, and their vacuoles are less filled with water, leading to a more stable
4 285 tissue structure.

5
6 286 The optical image of a rice root shows the main compartments: root hair; epidermis; cortex;
7
8 287 endodermis; and stele containing the vascular bundles and metaxylem vessels (Fig. 7a). The
9
10 288 example MS imaging measurement demonstrates the fine-scale localization of a penta-hexose
11 289 carbohydrate in the root cortex (Fig. 7b, red), and of a phosphatidylcholine mapped to the
12 290 epidermis and the central stele with a specific absence from metaxylem vessels (Fig. 7b,
13 291 green). The detected hexose is likely part of the carbohydrate reserves in root cortex. The
14
15 292 carbon metabolism generally represents an essential sink-source interaction, in which root and
16 293 shoot growth influence each other mutually. Consequently, the carbohydrates translocation
17 294 from leaves and their storage in roots are very sensitive to stresses, management practices and
18 295 root-microbe interactions. Decreased root reserves are known to profoundly affect plant
19 296 performance^{69, 70}. Thus, carbon use and sugar signaling are of high scientific interest and
20 297 represent a good example for the applicability of a plant metabolome atlas.

27 298 **2.6 Markers for *Fusarium* infection**

28 299 In cereal crops, *F. graminearum* (*Fg*) is a major agent of fungal diseases which cause severe
29 300 yield reductions and quality deterioration, especially due to mycotoxin accumulations in seeds
30 301 which are toxic to farm animals and humans⁷¹. Both the healthy and infected wheat seed have
31 302 low moisture content (< 20%). Infected wheat seed demonstrates the characteristic weight
32 303 reduction, shriveled and light-brown appearance due to colonization by *Fg*⁷² as shown in the
33 304 photographic (Fig. 8a, d) and microscopic images (Fig. 8b, e). The characteristic low moisture
34 305 content in healthy wheat seed and additionally the substantial disease-related physical
35 306 changes represent a specific challenge for the preparation of thin uniform sections from wheat
36 307 seed.

37 308 To meet this intrinsic problem, a tape-based method⁷³ was adapted, which assists the
38 309 generation of thin complete sections from hard specimens. A specially prepared adhesive
39 310 tape, functioning at low temperatures, was attached to the cut surface of sample to support the
40 311 sectioning. The seed surrounded by CMC as a block, which was formed by freezing CMC in a
41 312 mold using a cooling mixture. For a comparative MS imaging, healthy and diseased seed of
42 313 the highly *Fusarium* head blight (FHB) susceptible wheat cultivar Florence-Aurore were used.
43 314 The overlay ion images of a healthy (Fig. 8c) and an infected wheat bran (Fig. 8f) show
44 315 uniform distributions of a tetra-hexose metabolite in the endosperm (Fig. 8f, red). However,
45 316 several compounds were specifically detected in the bran of the infected seed, e.g. 4-

1
2
3 317 (trimethylammonio)but-2-enoate (Fig. 8f, green). This distribution indicates a relation to the
4 318 pathogen infection since *Fg* preferably colonizes this peripheral tissue in mature seeds⁷⁴. The
5
6 319 localization of *Fg* in this particular sample was confirmed by fluorescence microscopy (Fig.
7
8 320 S12). The chemical identity of the fungus-related metabolite (4-(trimethylammonio)but-2-
9
10 321 enoate) was confirmed by MS/MS analysis (Fig. S13f). MALDI MS spectra of *Fg* hyphae
11
12 322 also resulted in the same metabolite signals (Fig. S13e). In addition, a carnitine metabolite
13
14 323 was detected in the infected wheat bran (Fig. S13a, b) and in fungal hyphae (Fig. S13e). Both
15
16 324 metabolites belong to the carnitine metabolism, which is quite similar in plants and fungi.
17
18 325 However, they were identified from hyphae *in planta* (diseased wheat seed) and from hyphae
19
20 326 *in vitro* (culture medium). This indicates a fungal origin and thus, both were denoted as
21
22 327 pathogenesis-related metabolites.

23
24 328 As demonstrated here, MS imaging can be applied to detect candidates for pathogenesis-
25
26 329 related metabolites solely by their spatial distribution within infected parts of a tissue. Such
27
28 330 “biomarkers” could be applied to visualize unknown sites of host-pathogen interactions. The
29
30 331 few available metabolomic studies on interactions between biotic stressors and plants have
31
32 332 already demonstrated that those metabolic processes are highly specific for a given tissue,
33
34 333 specie and pathosystem. Therefore, it is conceivable that untargeted MS visualization of
35
36 334 metabolomic plant-pathogen interactions will lead to new insights into chemical plant defense
37
38 335 mechanisms.

39
40
41
42
43
44
45
46
47
48
49
50
51
52
53
54
55
56
57
58
59
60 336

337 **3 Experimental**

338 Detailed information on chemicals and origin of plant material can be found in the supporting
339 information, Methods S1, and Methods S2, respectively.

340 **3.1 Sample preparation for MALDI imaging**

341 We optimized sectioning procedures like embedding in different media, snapshot freezing,
342 use of adhesive tape and manual sectioning to obtain thin uniform sections. For
343 cryosectioning, water (ice) was used as an adhesive to hold the specimen on a sample holder
344 of a cryomicrotome (HM 525 cryostat, Thermo Scientific, Dreieich, Germany). Sections of
345 10-20 μm thickness were cut at -15 to -25 $^{\circ}\text{C}$. The sections were thaw-mounted on
346 microscope glass slides (75 x 25 x 1 mm), which were stored at -80 $^{\circ}\text{C}$ until analysis. Prior to
347 matrix application, sections were brought to room temperature in a desiccator to avoid
348 condensation of humidity on the sample surface. An Olympus BX-40 (Olympus Europa
349 GmbH, Hamburg, Germany) microscope was used to capture optical images of the sections
350 before and after matrix application. In case of positive ion mode, a solution of 200 μL
351 2,5-dihydroxybenzoic acid (DHB) (30 mg/mL in acetone:water (50:50, v/v), 0.1 %
352 trifluoroacetic acid), was applied. For negative ion mode, a solution of 200 μL 4-nitroaniline
353 (10 mg/mL in acetone:water (50:50, v/v)) was sprayed with a pneumatic sprayer⁷⁵. Specific
354 details on sample preparation for individual specimen are given in section 3.3.

355 **3.2 Instrumentation for MALDI imaging**

356 Highly resolved mass spectra were generated with a Fourier transform orbital trapping mass
357 spectrometer (Exactive or Q Exactive, Thermo Fisher Scientific GmbH, Bremen, Germany)
358 coupled to atmospheric-pressure scanning-microprobe matrix assisted laser
359 desorption/ionization imaging source (AP-SMALDI10, TransMIT GmbH, Giessen, Germany)
360^{76 29}. For desorption/ionization of the analyte a nitrogen laser (LTB MNL-106, LTB, Berlin,
361 Germany) with a repetition rate of 60 Hz and wavelength of 337 nm was used. The laser beam
362 was focused perpendicular to the sample to a laser ablation spot size of 5 μm . The samples
363 were scanned with 5 to 25 μm step size and the target voltage was set to 4.3 kV. The mass
364 spectrometer was operated in positive ion/negative ion mode and spectra were scanned in
365 different mass-to-charge (m/z) ranges and mass resolutions (R), with $m/z = 100$ -1500 and
366 $R=50,000$ to 140,000 respectively. Automatic gain control was disabled and the ion injection
367 time was set to 500 ms. Internal calibration was achieved by using lock masses from matrix

1
2
3 368 clusters. The cycle time for one pixel at 140,000 resolving power was 1.3 s. A detailed
4 369 description of measurements parameters for each sample is given below.
5
6
7

8 371 **3.3 Experimental details for individual specimen**

9 372 **Oil seed rapeseed**

10 373 Seeds are embedded in 4% (w/v) carboxymethyl cellulose (CMC) solution. Initially, seeds
11 374 were kept in Tissue-Tek[®] molds (15 x 15 x 5 mm) and the CMC solution was poured to
12 375 embed the seeds. To remove air bubbles, the filled mold was initially kept at -20 °C for 20
13 376 minutes, and thereafter transferred to -80 °C for 50 to 60 minutes, to form a solid block. These
14 377 blocks were transferred to a cryomicrotome at -20 °C to obtain thin tissue sections of 20 µm
15 378 thickness of oilseed rape at germination and maturation stage (Fig. 1a and Fig. 1b). MS
16 379 images for germinating seed were obtained at a pixel size of 10 µm with 225 x 357 pixels
17 380 (Fig. 1c and e). For the mature seed, MS images were obtained at a pixel size of 25 µm with
18 381 100 x 120 pixels (Fig. 1d and f). In both experiments, mass spectra were acquired with. The
19 382 resolution of the mass spectrometer was set to 50,000 @ m/z 200 for a mass range of m/z 150-
20 383 1000 in positive ion mode.
21
22
23
24
25
26
27
28
29

30 384 31 385 **Wheat seed**

32 386 In contrast to oilseed rape, wheat seeds were directly mounted without embedding in the
33 387 cryomicrotome, enabling tissue section preparation by direct cryosectioning at -25 °C to
34 388 obtain a 20 µm thick tissue section (Fig. 3a). For MS imaging measurements, an area of 1600
35 389 x 900 µm² (320 x 180 pixels) was scanned with a pixel size of 5 µm (Fig. 3b). The mass
36 390 spectrometer was set to a resolution of 70,000 @ m/z 200 for a mass range of m/z 400-1000 in
37 391 positive ion mode. For the negative ion mode measurement, an area of 2250 x 2250 µm² (150
38 392 x 150 pixels) was scanned with a pixel size of 15 µm (Fig. 4b). The mass spectrometer was
39 393 set to a resolution of 100,000 @ m/z 200 for a mass range of m/z 200-1000.
40
41
42
43
44
45
46
47
48

49 395 **Wheat spike rachis**

50 396 The spike rachis was fixed inside the tragacanth paste 15 % (w/v) and subsequently stored at -
51 397 80 °C for 30 min to obtain a solid block. The cryomicrotome was used to obtain sections of
52 398 10 µm thickness at -15 °C (Fig. 5a). After application of the matrix, an area of 2400 x 1000
53 399 µm² (240 x 100 pixels) was scanned with a step size of 10 µm (Fig. 5b). The mass
54
55
56
57
58
59
60

1
2
3 400 spectrometer was set to a resolution of 100,000 @ m/z 200 for a mass range of m/z 100-1000
4 401 in positive ion mode.
5
6

7 402

8 403 **Wheat stem**

9 404 Prior to sectioning, the stem base was frozen in a 4% (w/v) CMC solution by using a coolant
10 405 mixer for faster freezing (dry ice and hexane) due to high water content. After snap freezing,
11 406 the CMC block was transferred to the cryostat for sectioning, and sections of 20 μm thickness
12 407 were obtained at $-20\text{ }^\circ\text{C}$ (Fig. 6a), scanning an area of $1150 \times 1050\ \mu\text{m}^2$ (230 x 210 pixels)
13 408 with a step size of 10 μm (Fig. 6b). The mass spectrometer was set to a resolution of 70,000
14 409 @ m/z 200 for a mass range of m/z 250-1000 in positive ion mode.
15
16
17
18
19

20 410

21 411 **Rice roots**

22 412 Root cross sections were taken from the maturation zone of seminal roots. A common shaving
23 413 blade was used to obtain thin sections. Thereby, a root was held in between a halved
24 414 Styrofoam[®], and afterwards the blade was moved from top to bottom tangential to the
25 415 Styrofoam[®]. The obtained thin section was placed on a glass slide (Fig. 7a). MS imaging
26 416 analysis on root sections was performed in an area of $1100 \times 1200\ \mu\text{m}^2$ (110 x 120 pixels)
27 417 with 10 μm step size (Fig. 7b). The mass spectrometer was set to a resolution of 50,000 @
28 418 m/z 200 for a mass range of m/z 100-1200 in positive ion mode.
29
30
31
32
33
34

35 419

36 420 ***Fusarium graminearum* infected wheat seed**

37 421 Wheat seed were embedded in a 4% CMC solution followed by a snap freezing using a
38 422 coolant mixture (dry ice and hexane). Subsequently, the block was placed in a cryomicrotome
39 423 sample holder. Tissue sections of 20 μm thickness were obtained at $-20\text{ }^\circ\text{C}$. The adhesive tape
40 424 was kept over the trimmed sample. Then a uniform smooth surface was use to give light
41 425 pressure so that the adhesive tape stick to the surface of the sample. Then a twister was used
42 426 to hold the tape while the cryomicrotome blade was slowly moved to obtain the tissue section
43 427 on the adhesive tape (Fig 8b, e). Then the adhesive tape with the section was fixed on a glass
44 428 slide, using a double-sided tape. Matrix was applied on the tissue while the sample was
45 429 attached to the adhesive tape. In case of the healthy wheat seed, an area of $4100 \times 3400\ \mu\text{m}^2$
46 430 (205 x 170 pixels) was scanned with a step size of 20 μm (Fig. 8c). In case of the infected
47 431 seed, which is comparatively smaller in dimension, a step size of 15 μm was used (Fig. 8F).
48 432 In both cases, the mass resolution was set at 100,000 @ m/z 200 for a mass range of m/z 100-
49 433 1000 in positive ion mode.
50
51
52
53
54
55
56
57
58
59
60

434 3.4 Data processing and image generation

435 Ion images of selected m/z values were generated using the in-house developed MIRION
436 software package⁷⁷ with a m/z bin width of $\Delta m/z = \pm 5$ ppm. The ion images were normalized
437 to the highest intensity for each ion species separately. RGB images of three different m/z
438 values were overlaid and demonstrated simultaneously. Other data processing steps like
439 interpolation, smoothing or normalization to the matrix signals were not needed and were not
440 applied during the image generation process. The MS images in supporting information,
441 Fig. S6, were generated by converting the raw files from the Orbitrap instrument to imzML
442 format⁷⁸. Images were then generated with MSiReader version 0.04⁷⁹ in the batch processing
443 option, based on a predefined theoretical m/z value list. Mass accuracies for Table 1 and Table
444 S1 were calculated according to⁸⁰ using intensity-weighted average values from all spectra of
445 one image.

446 Literature and METLIN search was used to identify compounds. The compounds were
447 identified using high mass accuracy (< 2 ppm). For subsequent biological interpretation,
448 annotated metabolites were assigned to appropriate metabolome categories and pathways by
449 consulting the web applications KEGG Pathway Maps⁸¹, MetaCyc Pathway⁸², and LIPID
450 MAPS⁸³.

451

452 **4 Conclusions**

453 In this study, we present an approach for MS imaging of plant metabolites that covers
454 multiple mono- and dicot species, major plant organs and a wide variety of compound classes.
455 Results were in excellent agreement with previous knowledge including bulk sample MS
456 studies and in addition provided new information on the detailed spatial distribution of
457 important plant metabolites. In contrast to classical imaging methods, the analytes in MS
458 imaging do not have to be known upfront. All presented MS imaging measurements are based
459 on accurate mass determination (mass accuracy better than 2 ppm) for reliable identification,
460 and were performed at 5 to 25 μm pixel size in order to visualize small spatial features.
461 Previous MS imaging studies of plants were so far limited to a selected organ in a particular
462 species and focused on a certain compound class. In order to cover a wider range of plant
463 organs, we optimized different preparation methods, which were adapted for the
464 physicochemical properties of the varying plant organs and tissues. Figure 9 summarizes the
465 results presented in this manuscript and also includes additional plant tissues (distal root, leaf
466 and stem) which are discussed in the supplementary information (Fig. S11, S14, S15). This
467 demonstrates that MS imaging is now applicable to the entire plant from head to roots. It
468 covers all plant organs with relevance for current and future studies towards a comprehensive
469 understanding of physiological and molecular mechanisms behind complex traits and
470 environmental adaptations. One application is to investigate changes in metabolites during
471 plant development as shown for mature and germinating seed of oilseed rape. The detailed
472 localization of more than 90 compounds allowed assignments to certain metabolic processes
473 and first clues to functions in plant tissues. The wide range of analyzed compounds also
474 enabled to describe metabolic pathways, as demonstrated for example by the hitherto unseen
475 spatio-temporal distributions of 22 phenylpropanoids representing a metabolomic network
476 associated with sinapate esters which is considered a major component of oilseed rape meal
477 quality.
478 The ‘untargeted’ nature of MS imaging allows the detection of marker compounds for a
479 specific physiological status, for example to investigate or predict the quality of plant-
480 pathogen interactions. For Fusarium head blight, one of the most devastating diseases
481 affecting grain crops, fungus-specific compounds were detected in infected wheat seed and
482 their distribution matched with florescence labeling.

1
2
3 483 These examples demonstrate the wealth of information that can be obtained from high
4 484 resolution MS imaging of plant metabolites. If this approach is combined with classical LC-
5
6 485 MS/MS approaches and applied on a larger scale it could be used to build up an inventory of
7
8 486 the plant metabolome. The long-term goal would be to establish a plant metabolome atlas for
9
10 487 different species similar to the human proteome atlas ⁸⁴ or the *Drosophila melanogaster*
11 488 metabolome atlas ⁸⁵. Similar to the insect field, the first step would be to establish a
12
13 489 metabolome atlas for selected species, e.g. wheat as an important crop plant and *Arabidopsis*
14 490 *thaliana* as a frequently used plant model. The initial generation of a baseline tissue map as
15
16 491 initiated with the presented study would be an important step in this direction. Metabolites are
17
18 492 the end products of cellular processes and therefore, can provide comprehensive information
19
20 493 on a plant's physiological status. Therefore an atlas of biochemical networks can lead to novel
21 494 insights into metabolic capacities of cells ⁸⁶, or can be used as reference for profiling studies.
22
23 495 For example, in pathogen-interaction studies MS imaging data from infected plants (as shown
24
25 496 in section 2.6) could be compared with the atlas data to identify compounds which are
26
27 497 specific for this plant physiological status. In general this kind of information can be used as a
28
29 498 reference to investigate systemic and local effects of stress (biotic or abiotic), developmental
30
31 499 stages as well as wildtype/genotype studies. In addition, the distribution of these markers
32
33 500 could give a first indication about their functional role.
34
35 501 Therefore the authors are convinced that high resolution MS imaging will provide new
36
37 502 valuable insights in many areas of plant research in the future.
38
39
40
41
42
43
44
45
46
47
48
49
50
51
52
53
54
55
56
57
58
59
60

504 **Acknowledgements**

505 The author would like to acknowledge Fateme Mirzajani (Department of Phytochemistry,
506 Shahid Beheshti University, Iran) for the rice root samples and Christian Obermeier,
507 (Department of Plant Breeding, IFZ, Justus Liebig University Giessen, Germany) for
508 providing seeds and stem of oilseed rape. This work was funded by the Hessian Ministry of
509 Science and Arts (HMWK) through LOEWE focus "*Ambiprobe*" and by the Deutsche
510 Forschungsgemeinschaft DFG Sp314/13-1.

511

512 **References**

- 513 1. R. M. Pérez-Clemente, V. Vives, S. I. Zandalinas, M. F. López-Climent, V. Muñoz and A.
514 Gómez-Cadenas, *BioMed research international*, 2013, **2013**, 654120.
- 515 2. R. A. Dixon and D. Strack, *Phytochemistry*, 2003, **62**, 815-816.
- 516 3. R. Nakabayashi and K. Saito, *Analytical and bioanalytical chemistry*, 2013, **405**, 5005-5011.
- 517 4. N. Carreno-Quintero, H. J. Bouwmeester and J. J. Keurentjes, *Trends Genet*, 2013, **29**, 41-50.
- 518 5. C. Brunetti, R. M. George, M. Tattini, K. Field and M. P. Davey, *Journal of experimental*
519 *botany*, 2013, **64**, 4011-4020.
- 520 6. T. Obata and A. R. Fernie, *Cellular and molecular life sciences : CMLS*, 2012, **69**, 3225-3243.
- 521 7. D. Balmer, V. Flors, G. Glauser and B. Mauch-Mani, *Frontiers in plant science*, 2013, **4**, 82.
- 522 8. G. J. Patti, O. Yanes and G. Siuzdak, *Nature Reviews Molecular Cell Biology*, 2012, **13**, 263-
523 269.
- 524 9. T. Neuberger, H. Rolletschek, A. Webb and L. Borisjuk, in *Lipidomics*, ed. D. Armstrong,
525 Humana Press, 2009, vol. 579, ch. 24, pp. 485-496.
- 526 10. S. L. Shaw and D. W. Ehrhardt, *Annual Review of Plant Biology*, 2013, **64**, 351-375.
- 527 11. Y. J. Lee, D. C. Perdian, Z. Song, E. S. Yeung and B. J. Nikolau, *The Plant Journal*, 2012, **70**,
528 81-95.
- 529 12. A. K. Mullen, M. R. Clench, S. Crosland and K. R. Sharples, *Rapid Communications in Mass*
530 *Spectrometry*, 2005, **19**, 2507-2516.
- 531 13. S. Robinson, K. Warburton, M. Seymour, M. Clench and J. Thomas-Oates, *New Phytologist*,
532 2007, **173**, 438-444.
- 533 14. Y. Yoshimura, N. Zaima, T. Moriyama and Y. Kawamura, *PLoS ONE*, 2012, **7**, e31285.
- 534 15. N. Zaima, N. Goto-inoue, T. Hayasaka and M. Setou, 2010, 2723-2729.
- 535 16. J. H. Jun, Z. Song, Z. Liu, B. J. Nikolau, E. S. Yeung and Y. J. Lee, *Analytical Chemistry*,
536 2010, **82**, 3255-3265.
- 537 17. R. Shroff, F. Vergara, A. Muck, A. Svatos and J. Gershenzon, *Proceedings of the National*
538 *Academy of Sciences*, 2008, **105**, 6196-6201.
- 539 18. V. Vrkslav, A. Muck, J. Cvačka and A. Svatoš, *Journal of the American Society for Mass*
540 *Spectrometry*, 2010, **21**, 220-231.
- 541 19. J. Sarsby, M. W. Towers, C. Stain, R. Cramer and O. A. Koroleva, *Phytochemistry*, 2012, **77**,
542 110-118.
- 543 20. M. Peukert, A. Matros, G. Lattanzio, S. Kaspar, J. Abadía and H.-P. Mock, *New Phytologist*,
544 2012, **193**, 806-815.
- 545 21. P. Franceschi, Y. Dong, K. Strupat, U. Vrhovsek and F. Mattivi, *Journal of Experimental*
546 *Botany*, 2012, **63**, 1123-1133.
- 547 22. P. J. Horn, A. R. Korte, P. B. Neogi, E. Love, J. Fuchs, K. Strupat, L. Borisjuk, V. Shulaev, Y.
548 J. Lee and K. D. Chapman, *The Plant Cell Online*, 2012, **24**, 622-636.
- 549 23. A. R. Korte, Z. Song, B. J. Nikolau and Y. J. Lee, *Analytical Methods*, 2012, **4**, 474.
- 550 24. R. J. R. Jaeger, M. Lamshöft, S. Gottfried, M. Spiteller and P. Spiteller, *Journal of Natural*
551 *Products*, 2013, **76**, 127-134.
- 552 25. N. Goto-Inoue, M. Setou and N. Zaima, *Analytical Sciences*, 2010, **26**, 821-825.
- 553 26. P. J. Horn, J. E. Silva, D. Anderson, J. Fuchs, L. Borisjuk, T. J. Nazareus, V. Shulaev, E. B.
554 Cahoon and K. D. Chapman, *The Plant journal : for cell and molecular biology*, 2013, **76**, 138-
555 150.
- 556 27. A. Korte, M. Yandeu-Nelson, B. Nikolau and Y. Lee, *Anal Bioanal Chem*, 2015, **407**, 2301-
557 2309.
- 558 28. D. Holscher, R. Shroff, K. Knop, M. Gottschaldt, A. Crecelius, B. Schneider, D. G. Heckel, U.
559 S. Schubert and A. Svatos, *Plant J.*, 2009, **60**, 907-918.
- 560 29. A. Römpf, S. Guenther, Y. Schober, O. Schulz, Z. Takats, W. Kummer and B. Spengler,
561 *Angew. Chem.-Int. Edit.*, 2010, **49**, 3834-3838.
- 562 30. A. Römpf and B. Spengler, *Histochemistry and Cell Biology*, 2013, **139**, 759-783.
- 563 31. A. Berisha, S. Dold, S. Guenther, N. Desbenoit, Z. Takats, B. Spengler and A. Römpf, *Rapid*
564 *Commun. Mass Spectrom.*, 2014, **28**, 1779-1791.
- 565 32. D. Bhandari, T. Shen, A. Römpf, H. Zorn and B. Spengler, *Analytical and Bioanalytical*
566 *Chemistry*, 2014, **406**, 695-704.
- 567 33. B. Li, D. R. Bhandari, C. Janfelt, A. Römpf and B. Spengler, *The Plant Journal*, 2014, **80**, 161-
568 171.
- 569 34. K. Wolfram, J. Schmidt, V. Wray, C. Milkowski, W. Schliemann and D. Strack, *Phytochemistry*,
570 2010, **71**, 1076-1084.

- 1
2
3 571 35. M. J. Holdsworth, W. E. Finch-Savage, P. Grappin and D. Job, *Trends in plant science*, 2008,
4 572 **13**, 7-13.
5 573 36. R. Angelovici, G. Galili, A. R. Fernie and A. Fait, *Trends in plant science*, 2010, **15**, 211-218.
6 574 37. P. Koehler, G. Hartmann, H. Wieser and M. Rychlik, *Journal of Agricultural and Food*
7 575 *Chemistry*, 2007, **55**, 4678-4683.
8 576 38. U. Thiyam, P. Claudia, U. Jan and B. Alfred, *European Food Research and Technology*, 2009,
9 577 **229**, 825-831.
10 578 39. J. Fang, M. Reichelt, W. Hidalgo, S. Agnolet and B. Schneider, *PloS one*, 2012, **7**, e48006.
11 579 40. A. Baumert, C. Milkowski, J. Schmidt, M. Nimtz, V. Wray and D. Strack, *Phytochemistry*, 2005,
12 580 **66**, 1334-1345.
13 581 41. D. Meissner, A. Albert, C. Böttcher, D. Strack and C. Milkowski, *Planta*, 2008, **228**, 663-674.
14 582 42. P. Burchard, W. Bilger and G. Weissenböck, *Plant, Cell & Environment*, 2000, **23**, 1373-1380.
15 583 43. K. Clauss, E. von Roepenack-Lahaye, C. Böttcher, M. R. Roth, R. Welti, A. Erban, J. Kopka,
16 584 D. Scheel, C. Milkowski and D. Strack, *Plant Physiology*, 2011, **155**, 1127-1145.
17 585 44. J. Mittasch, C. Böttcher, A. Frolov, D. Strack and C. Milkowski, *Plant physiology*, 2013, **161**,
18 586 1656-1669.
19 587 45. L. Borisjuk, T. Neuberger, J. Schwender, N. Heinzl, S. Sunderhaus, J. Fuchs, J. O. Hay, H.
20 588 Tschiersch, H.-P. Braun, P. Denolf, B. Lambert, P. M. Jakob and H. Rolletschek, *The Plant*
21 589 *cell*, 2013, **25**, 1625-1640.
22 590 46. A. Hüsken, A. Baumert, D. Strack, H. C. Becker, C. Möllers and C. Milkowski, *Molecular*
23 591 *Breeding*, 2005, **16**, 127-138.
24 592 47. M. Noda and M. Matsumoto, *Biochimica et Biophysica Acta (BBA) - Lipids and Lipid*
25 593 *Metabolism*, 1971, **231**, 131-133.
26 594 48. B. Manning, K. Schulze and T. McNee, in *Wheat growth & development*
27 595 eds. J. White and J. Edwards, NSW Department of Primary Industries 2007, pp. 71-86.
28 596 49. J. B. Harborne and C. A. Williams, *Phytochemistry*, 2000, **55**, 481-504.
29 597 50. R. Tanoue, M. Kobayashi, K. Katayama, N. Nagata and H. Wada, *FEBS Letters*, 2014, **588**,
30 598 1680-1685.
31 599 51. X. Wang, *Current opinion in plant biology*, 2004, **7**, 329-336.
32 600 52. H. Xue, X. Chen and G. Li, *Current opinion in plant biology*, 2007, **10**, 483-489.
33 601 53. J. A. Engelman, J. Luo and L. C. Cantley, *Nature reviews. Genetics*, 2006, **7**, 606-619.
34 602 54. J. Liu, J. Zhou and D. Xing, *PloS one*, 2012, **7**, e33817.
35 603 55. F. Brignole-Baudouin, N. Desbenoit, G. Hamm, H. Liang, J.-P. Both, A. Brunelle, I. Fournier,
36 604 V. Guerineau, R. Legouffe, J. Stauber, D. Touboul, M. Wisztorski, M. Salzet, O. Laprevote and
37 605 C. Baudouin, *Plos One*, 2012, **7**, e50180.
38 606 56. R. Metzner, M. R. Thorpe, U. Breuer, P. Blumler, U. Schurr, H. U. Schneider and W. H.
39 607 Schroeder, *Plant Cell Environ*, 2010, **33**, 1393-1407.
40 608 57. N. A. Brown, C. Bass, T. K. Baldwin, H. Chen, F. Massot, P. W. Carion, M. Urban, A. M. van
41 609 de Meene and K. E. Hammond-Kosack, *J Pathog*, 2011, **2011**, 626345.
42 610 58. Z. Magbanua, W. Williams and D. Luthe, 2013.
43 611 59. N. A. Brown, M. Urban, A. M. van de Meene and K. E. Hammond-Kosack, *Fungal Biol*, 2010,
44 612 **114**, 555-571.
45 613 60. Y. Saga and H. Tamiaki, *Chemistry & Biodiversity*, 2012, **9**, 1659-1683.
46 614 61. L. C. van Loon, M. Rep and C. M. J. Pieterse, *Annual Review of Phytopathology*, 2006, **44**,
47 615 135-162.
48 616 62. A. M. Mudge, R. Dill-Macky, Y. Dong, D. M. Gardiner, R. G. White and J. M. Manners,
49 617 *Physiological and Molecular Plant Pathology*, 2006, **69**, 73-85.
50 618 63. S. Gottwald, B. Samans, S. Lück and W. Friedt, *BMC Genomics*, 2012, **13**, 1-22.
51 619 64. C. Tayeh, B. Randoux, F. Laruelle, N. Bourdon, D. Renard-Merlier and P. Reignault, *Lipids as*
52 620 *Markers of Induced Resistance in Wheat: A Biochemical and Molecular Approach*, 2013.
53 621 65. J. Raaijmakers, T. Paulitz, C. Steinberg, C. Alabouvette and Y. Moënné-Loccoz, *Plant Soil*,
54 622 2009, **321**, 341-361.
55 623 66. S. E. Smith and F. A. Smith, *Mycologia*, 2012, **104**, 1-13.
56 624 67. J. S. Singh, V. C. Pandey and D. P. Singh, *Agriculture, Ecosystems & Environment*, 2011,
57 625 **140**, 339-353.
58 626 68. J. Shen, C. Li, G. Mi, L. Li, L. Yuan, R. Jiang and F. Zhang, *J Exp Bot*, 2013, **64**, 1181-1192.
59 627 69. Y. L. Ruan, *Annual review of plant biology*, 2014, **65**, 33-67.
60 628 70. L. V. Kravchenko, A. I. Shapozhnikov, N. M. Makarova, T. S. Azarova, K. A. L'vova, I. I.
61 629 Kostyuk, O. A. Lyapunova and I. A. Tikhonovich, *Russ J Plant Physiol*, 2011, **58**, 936-940.
62 630 71. K. Kazan, D. M. Gardiner and J. M. Manners, *Mol Plant Pathol*, 2012, **13**, 399-413.
63 631 72. S. Walter, P. Nicholson and F. M. Doohan, *New Phytol*, 2010, **185**, 54-66.

- 1
2
3 632 73. T. Kawamoto, *Archives of Histology and Cytology*, 2003, **66**, 123-143.
4 633 74. E. M. Del Ponte, J. M. C. Fernandes and G. C. Bergstrom, *Journal of Phytopathology*, 2007,
5 634 **155**, 577-581.
6 635 75. W. Bouschen, O. Schulz, D. Eikel and B. Spengler, *Rapid Commun Mass Sp*, 2010, **24**, 355-
7 636 364.
8 637 76. M. Koestler, D. Kirsch, A. Hester, A. Leisner, S. Guenther and B. Spengler, *Rapid Commun.*
9 638 *Mass Spectrom.*, 2008, **22**, 3275-3285.
10 639 77. C. Paschke, A. Leisner, A. Hester, K. Maass, S. Guenther, W. Bouschen and B. Spengler, *J*
11 640 *Am Soc Mass Spectrom*, 2013, **24**, 1296-1306.
12 641 78. T. Schramm, A. Hester, I. Klinkert, J.-P. Both, R. M. A. Heeren, A. Brunelle, O. Lapr evote, N.
13 642 Desbenoit, M.-F. Robbe, M. Stoeckli, B. Spengler and A. R ompp, *J. Proteomics*, 2012, **75**,
14 643 5106-5110.
15 644 79. G. Robichaud, K. P. Garrard, J. A. Barry and D. C. Muddiman, *Journal of the American*
16 645 *Society for Mass Spectrometry*, 2013, **24**, 718-721.
17 646 80. A. G. Brenton and A. R. Godfrey, *J. Am. Soc. Mass Spectrom.*, 2010, **21**, 1821-1835.
18 647 81. M. Kanehisa, S. Goto, S. Kawashima, Y. Okuno and M. Hattori, *Nucleic Acids Research*,
19 648 2004, **32**, D277-D280.
20 649 82. R. Caspi, T. Altman, K. Dreher, C. A. Fulcher, P. Subhraveti, I. M. Keseler, A. Kothari, M.
21 650 Krummenacker, M. Latendresse, L. A. Mueller, Q. Ong, S. Paley, A. Pujar, A. G. Shearer, M.
22 651 Travers, D. Weerasinghe, P. Zhang and P. D. Karp, *Nucleic Acids Research*, 2012, **40**, D742-
23 652 753.
24 653 83. E. Fahy, M. Sud, D. Cotter and S. Subramaniam, *Nucleic Acids Research*, 2007, **35**, W606-
25 654 612.
26 655 84. M. Uhlen, P. Oksvold, L. Fagerberg, E. Lundberg, K. Jonasson, M. Forsberg, M. Zwahlen, C.
27 656 Kampf, K. Wester, S. Hober, H. Wernerus, L. Bjorling and F. Ponten, *Nat Biotech*, 2010, **28**,
28 657 1248-1250.
29 658 85. V. R. Chintapalli, M. Al Bratty, D. Korzekwa, D. G. Watson and J. A. Dow, *PLoS One*, 2013, **8**,
30 659 e78066.
31 660 86. M. Arita, *Proc Natl Acad Sci U S A*, 2004, **101**, 1543-1547.
32 661
33 662
34
35
36
37
38
39
40
41
42
43
44
45
46
47
48
49
50
51
52
53
54
55
56
57
58
59
60

1
2
3 663 **Fig. 1** Comparative Mass spectrometry imaging of oilseed rape at maturation and early
4 664 germination stage. Optical images of seeds at (a) the early germination and (b) the maturation
5 665 stage: root tip (RT) containing the root apical meristem (RAM); epidermis tissue (Ep),
6 666 parenchyma tissue (Pa); vascular tissue (Va); shoot apical meristem (SAM); seed coat (S);
7 667 endosperm (E); putative nucellar tissue (NT); outer and inner cotyledon (OC and IC); abEp
8 668 (abaxial cotyledon epidermis); adEp (adaxial cotyledon epidermis); hypocotyl (H); radicle
9 669 (R); hypocotyl-radicle region (HR); and the seed coat-endosperm region (SE). Scale bar, 500
10 670 μm . Overlay of m/z images from early germinating (c) and mature (d) seeds showing the
11 671 tissue- and stage-specific spatial distributions of the cyclic spermidine conjugate $[\text{M}+\text{H}]^+$, m/z
12 672 496.24421 (red); the sinapoly glucose $[\text{M}+\text{H}-\text{H}_2\text{O}]^+$, m/z 369.11801 (green); and sinapine
13 673 $[\text{M}+\text{H}]^+$, m/z 310.16490 (blue). Overlay of ion images from early germinating (e) and mature
14 674 (f) seeds showing the tissue- and stage-specific spatial distributions of the tricaffeoyl
15 675 spermidine $[\text{M}+\text{K}]^+$, m/z 534.20009 (red); feruloylcholine FC(4-O-8')G $[\text{M}+\text{H}]^+$, m/z
16 676 476.22789 (green); and the phenolic choline ester UC#1 $[\text{M}+\text{H}]^+$, m/z 328.24824 (blue). (g)
17 677 Single pixel MS spectrum obtained at 10 μm pixel size measurement in the early germinating
18 678 seed. Different classes of compounds, such as sinapine, carbohydrate and lipids were
19 679 identified based on high mass accuracy. (h) On tissue MS/MS of sinapine from a 10 μm pixel.
20 680 R = mass resolution.
21
22
23
24
25
26
27
28
29
30
31
32
33
34
35
36
37
38
39
40
41
42
43
44
45
46
47
48
49
50
51
52
53
54
55
56
57
58
59
60

1
2
3 682 **Fig. 2** Scheme of metabolomic network associated with sinapate ester metabolism, localized
4 683 by high-resolution MS imaging in mature and early germinating oilseed rape. Spatial
5 684 distributions are shown in the ion images below the respective metabolites (left image: mature
6 685 seed; right image early germinating seed). Blue boxes marked by a white cross indicate that
7 686 the metabolite has not been detected at that developmental seed stage. Localized key
8 687 metabolites are marked in bold letters. The sinapate ester metabolism is highlighted as a grey
9 688 box. The shikimate pathway as gateway to the displayed branch of phenylpropanoid
10 689 metabolism is indicated as light blue box. The scheme was redrawn based on Clauss et al. ⁴³.
11 690 Abbreviations: G, guaiacyl moiety; Glc, glucoside; Hex, unknown hexose moieties
12 691 (commonly Glc); S, syringyl moiety; Soph, sophorose.
13
14
15
16
17
18
19
20

21 693 **Fig. 3** Mass spectrometry imaging of a wheat seed section at the soft dough stage with
22 694 different mass and spatial resolutions. (a) Optical image of a 20 μm cross section taken from
23 695 the germ. The image shows the coleoptile/coleorhiza (Co), the scutellum (Sc), and the
24 696 pericarp-seed coat region (PS). Scale bar, 500 μm . (b) Overlay of three ion images generated
25 697 with high mass resolution (± 5 ppm) and high spatial resolution (5 μm). The overlay shows
26 698 the tissue-specific spatial distributions of a polyphenol glycoside $[\text{M}+\text{K}]^+$, m/z 603.11107
27 699 (green) in the protection sheath coleoptile/coleorhiza covering the main compartments shoot,
28 700 plumules (first true leaves) and radicle; a phosphatidylcholine $[\text{PC}(36:4)+\text{K}]^+$, m/z 820.52531
29 701 (blue) in the scutellum (monocot cotyledon); and a phosphatidylglycerol $[\text{PG}(38:2)-\text{H}_2\text{O}+\text{H}]^+$,
30 702 m/z 785.56910 (red) in the pericarp-seed coat region. MS images were acquired in positive
31 703 ion mode with 320 x 180 pixels; 5 μm pixel size; and m/z bin width: $\Delta m/z = \pm 5$ ppm. (c)
32 704 Overlay of three ion images generated with high mass resolution (± 5 ppm) and low spatial
33 705 resolution (50 μm pixel size) resulting in a loss of spatial information. (d) Overlay of three
34 706 ion images generated with low mass resolution ($\Delta m/z = 0.1$ bin width) and high spatial
35 707 resolution (5 μm) resulting in a much less distinct resolution, due to neighboring peaks of
36 708 similar masses which interfere the image generation.
37
38
39
40
41
42
43
44
45
46
47
48
49

50 710 **Fig. 4** Mass spectrometry imaging in negative ion mode of wheat seed at soft dough stage. (a)
51 711 The optical image of the 20 μm seed cross section shows the coleoptile/coleorhiza (Co),
52 712 scutellum (Sc), the endosperm (E), the pericarp-seed coat region (PS), and crease (Cr). Scale
53 713 bar 500 μm . (b) Overlay of ion images shows the tissue-specific spatial distributions of a
54 714 polyphenol glycoside $[\text{M}-\text{H}]^-$, m/z 563.14063 (green) detected in the embryonic protection
55
56
57
58
59
60

1
2
3 715 sheath coleoptile/coleorhiza covering the main compartments shoot, plumules (first true
4 716 leaves) and radicle; and a phosphatidylinositol [PI(34:2)-H]⁻, *m/z* 833.51855 (red) located in
5
6 717 the scutellum and endosperm, but absent from the crease. MS images were generated with
7
8 718 150 x 150 pixels; 15 μm pixel size; *m/z* bin width: $\Delta m/z = \pm 5$ ppm.
9

10 719

11 **Fig. 5** Mass spectrometry imaging of a wheat rachis section at soft dough stage. (a) Optical
12 720 image of a 10 μm rachis cross section taken under UV-light. The section was obtained from
13 721 the center section of inflorescence and shows the epidermis (Ep) and the vascular bundles
14 722 (Vb) as round inclusions within the central parenchyma cells (Pa). Scale bar 500 μm. (b)
15 723 Overlay of ion images showing the tissue-specific distributions of a polyphenol glycoside
16 724 [M+H]⁺, *m/z* 565.15518 (green) in the epidermis; a lysophosphatidylcholine
17 725 [lysoPC(16:0)+K]⁺, *m/z* 534.29565 (blue) in the parenchyma; and a pheophytin [pheophytin
18 726 a+K]⁺, *m/z* 909.52908 (red) observed in the parenchyma and epidermis. MS images were
19 727 generated with 240 x 100 pixels; 10 μm pixel size; *m/z* bin width: $\Delta m/z = \pm 5$ ppm.
20 728
21
22
23
24
25
26
27

28 729

29 **Fig. 6** MS imaging of a wheat crown at seedling stage. (a) The optical image of a 20 μm
30 730 crown cross section shows the attached leaf sheath (LS) and the anatomy of seedling stem
31 731 comprising the epidermis (Ep); the cortex (Co); and the pith (Ph) as central portion including
32 732 the vascular bundles (Vb). Scale bar 500 μm. (b) Overlay of ion images showing the spatial
33 733 distributions of a polyphenol glycoside [M+K]⁺, *m/z* 565.15518 (red) the leaf sheath; and a
34 734 phosphatidylcholine [PC(36:4)+K]⁺, *m/z* 820.52531 (green) enriched in the vascular tissues
35 735 and evenly spread within the cortex. MS images were generated with 230 x 210 pixels; 5 μm
36 736 pixel size; *m/z* bin width: $\Delta m/z = \pm 5$ ppm.
37 737
38
39
40
41
42

43 738

44
45 **Fig. 7** Mass spectrometry imaging of a seminal rice root. (a) Optical image of a cross section
46 740 of a seminal root taken from a region proximal to stem (maturation zone). The image shows
47 741 the root hairs (Rh) attached to the epidermis (Ep); the central cortex (Co); the endodermis
48 742 (En) which separates a central root column (stele) containing the vascular bundles (Vb) and
49 743 the metaxylem vessels (Mx). The holes visible in the cortex are artefacts caused by the drying
50 744 of root section in the desiccator. Scale bar 500 μm. (b) Overlay of ion images showing the
51 745 spatial distributions of a [Penta-hexose+K]⁺, *m/z* 867.23784 (red) in the cortical layer, and a
52 746 phosphatidylcholine[PC(36:4)+K]⁺, *m/z* 820.52531 (green) in the epidermis and the entire
53
54
55
56
57
58
59
60

1
2
3 747 stele, except the metaxylem vessels. MS images were generated with 110 x 120 pixels; 10 μm
4 748 pixel size; m/z bin width: $\Delta m/z = \pm 5\text{ppm}$.

5
6
7 749

8
9 750 **Fig. 8** Comparative Mass spectrometry imaging of uninfected and *F. graminearum*-infected
10 751 wheat seeds at ripening stage. The photographic images show a healthy seed (**a**) and a seed
11 752 infected by the fungal pathogen *F. graminearum* (**d**) a causal agent of the head blight disease.
12 753 The seeds were sampled from the highly FHB susceptible spring wheat cv. Florence-Aurore.
13 754 Scale bars 500 μm . The optical images show 20 μm transverse sections of a healthy (**b**) and
14 755 infected seed (**e**), which were prepared by using the Kuwamoto method. Scale bars 500 μm .
15 756 Both the photographic (**d**) and the optical image (**e**) of the infected seed demonstrate the
16 757 characteristic weight reduction, shriveled and light-brown appearance associated with a highly
17 758 susceptible reaction to the FHB disease. The overlay of ion images of healthy (**c**) and infected
18 759 seed (**f**) show the spatial distribution of a [tetra-hexose+K]⁺ metabolite, m/z 705.18502 (red)
19 760 in the entire endosperm. In contrast, the metabolite 4-(trimethylammonio)but-2-enoate
20 761 [M+K]⁺, m/z 182.05779 (green) located in the entire seed bran and germ was only detected in
21 762 *F. graminearum* infected seeds. MS images of healthy seed were generated with 205 x 170
22 763 pixels; 20 μm pixel size; m/z bin width: $\Delta m/z = \pm 5\text{ppm}$. MS images of infected seed were
23 764 generated with 155 x 105 pixels; 15 μm pixel size; m/z bin width: $\Delta m/z = \pm 5\text{ppm}$.

24
25
26
27
28
29
30
31
32
33
34
35 765

36
37 766 **Fig. 9** Overview on the different plant structures which have been made available to high-
38 767 resolution MS imaging. Scale bars in all images 500 μm . (a) Sketch of a plant. (b) MS image
39 768 of wheat inflorescence rachis measured at 10 μm pixel size, details are given in Fig. 5. (c) MS
40 769 image of a seminal proximal rice root (maturation zone) measured at 10 μm pixel size; details
41 770 are given in Fig. 7. (d) MS image of a seminal distal rice root (elongation zone) measured at
42 771 10 μm pixel size, details are given in Supporting information, Fig. S11. (e) MS image of a
43 772 wheat leaf blade measured at 10 μm pixel size, details are given in Supporting information,
44 773 Fig. S14. (f) MS image of germinating oilseed rape at 10 μm pixel size, details are given in
45 774 Fig. 1. (g) MS image of oilseed rape stem at 20 μm pixel size, details are given in Supporting
46 775 information, Fig. S15. (h) MS image of wheat stem base at 5 μm pixel size, detail are given in
47 776 Fig. 6.

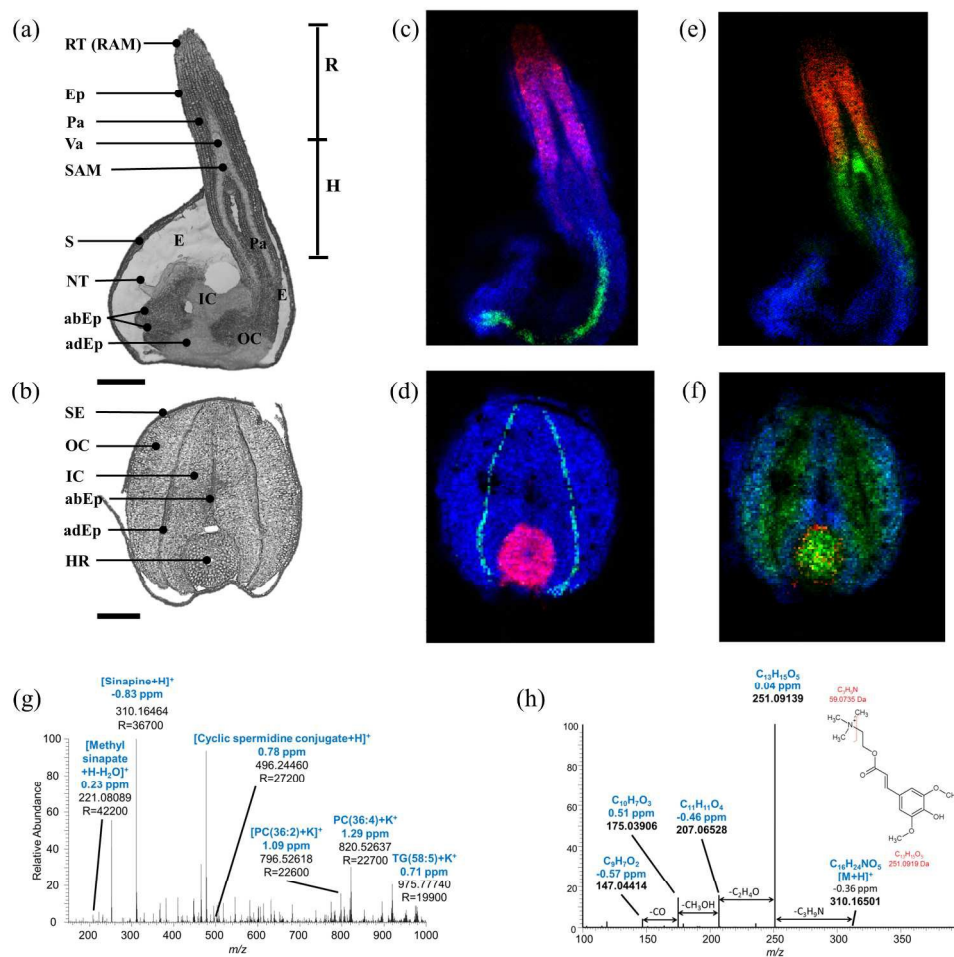


Fig. 1 Comparative Mass spectrometry imaging of oilseed rape at maturation and early germination stage. Optical images of seeds at (a) the early germination and (b) the maturation stage: root tip (RT) containing the root apical meristem (RAM); epidermis tissue (Ep), parenchyma tissue (Pa); vascular tissue (Va); shoot apical meristem (SAM); seed coat (S); endosperm (E); putative nucellar tissue (NT); outer and inner cotyledon (OC and IC); abEp (abaxial cotyledon epidermis); adEp (adaxial cotyledon epidermis); hypocotyl (H); radicle (R); hypocotyl-radicle region (HR); and the seed coat-endosperm region (SE). Scale bar, 500 μm . Overlay of m/z images from early germinating (c) and mature (d) seeds showing the tissue- and stage-specific spatial distributions of the cyclic spermidine conjugate $[M+H]^+$, m/z 496.24421 (red); the sinapoly glucose $[M+H-H_2O]^+$, m/z 369.11801 (green); and sinapine $[M+H]^+$, m/z 310.16490 (blue). Overlay of ion images from early germinating (e) and mature (f) seeds showing the tissue- and stage-specific spatial distributions of the tricaffeoyl spermidine $[M+K]^+$, m/z 534.20009 (red); feruloylcholine FC(4-O-8')G $[M+H]^+$, m/z 476.22789 (green); and the phenolic choline ester UC#1 $[M+H]^+$, m/z 328.24824 (blue). (g) Single pixel MS spectrum obtained at 10 μm pixel size measurement in the early germinating seed. Different classes of compounds, such as sinapine, carbohydrate and lipids were identified based on high mass accuracy. (h) On tissue MS/MS of sinapine from a 10 μm pixel. R = mass resolution. 255x251mm (260 x 260 DPI)

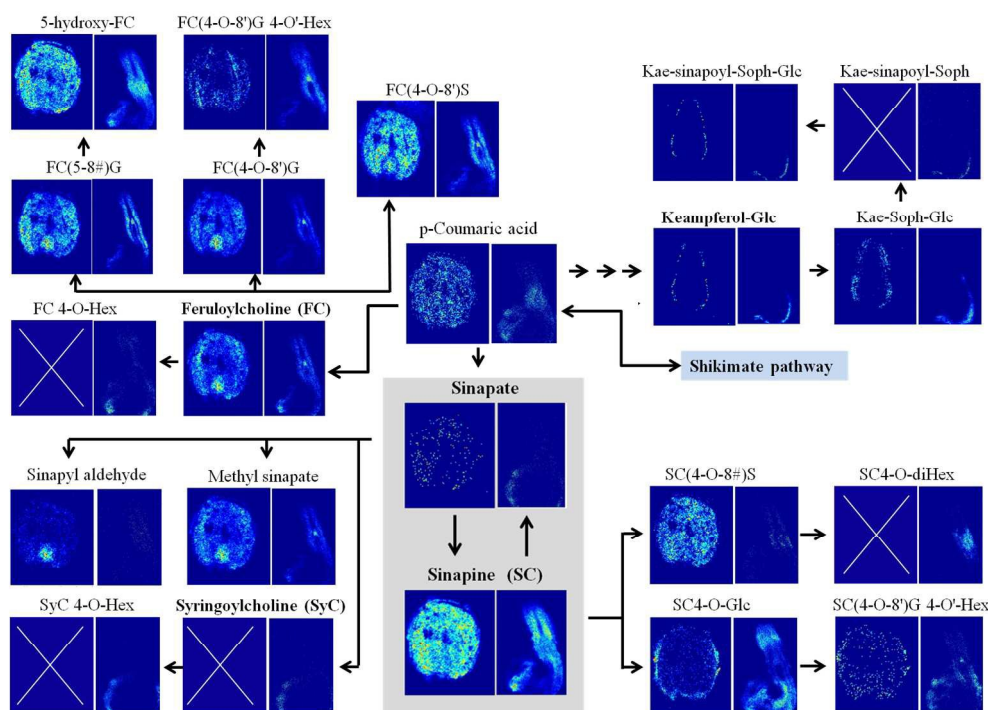


Fig. 2 Scheme of metabolomic network associated with sinapate ester metabolism, localized by high-resolution MS imaging in mature and early germinating oilseed rape. Spatial distributions are shown in the ion images below the respective metabolites (left image: mature seed; right image early germinating seed).

Blue boxes marked by a white cross indicate that the metabolite has not been detected at that developmental seed stage. Localized key metabolites are marked in bold letters. The sinapate ester metabolism is highlighted as a grey box. The shikimate pathway as gateway to the displayed branch of phenylpropanoid metabolism is indicated as light blue box. The scheme was redrawn based on Clauss et al. 43. Abbreviations: G, guaiacyl moiety; Glc, glucoside; Hex, unknown hexose moieties (commonly Glc); S, syringyl moiety; Soph, sophorose.

254x190mm (300 x 300 DPI)

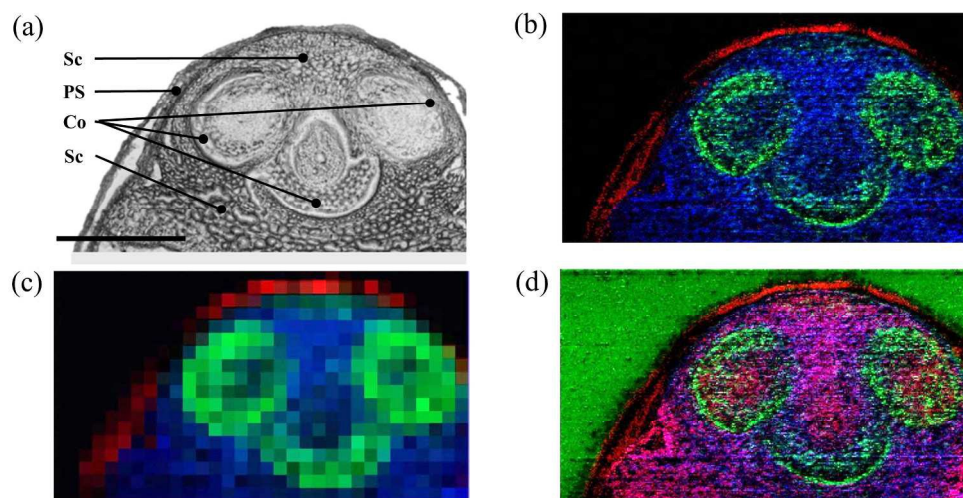
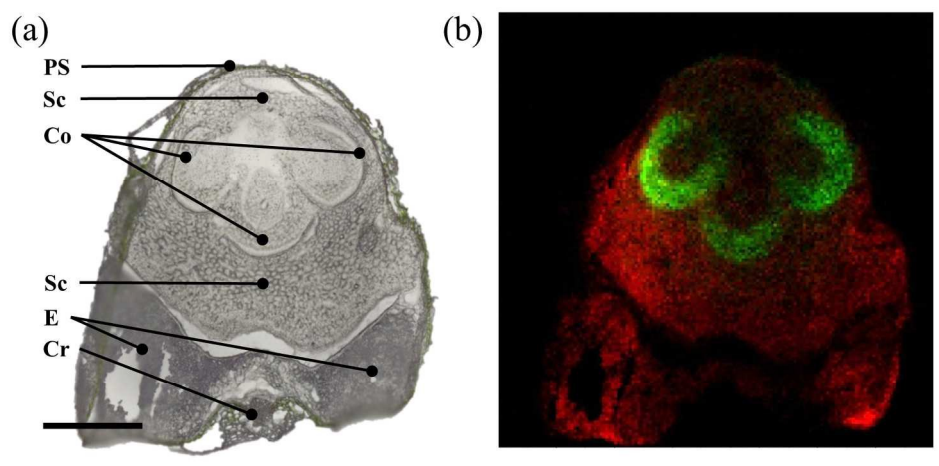


Fig. 3 Mass spectrometry imaging of a wheat seed section at the soft dough stage with different mass and spatial resolutions. (a) Optical image of a 20 μm cross section taken from the germ. The image shows the coleoptile/coleorhiza (Co), the scutellum (Sc), and the pericarp-seed coat region (PS). Scale bar, 500 μm . (b) Overlay of three ion images generated with high mass resolution (± 5 ppm) and high spatial resolution (5 μm). The overlay shows the tissue-specific spatial distributions of a polyphenol glycoside [M+K]⁺, m/z 603.11107 (green) in the protection sheath coleoptile/coleorhiza covering the main compartments shoot, plumules (first true leaves) and radicle; a phosphatidylcholine [PC(36:4)+K]⁺, m/z 820.52531 (blue) in the scutellum (monocot cotyledon); and a phosphatidylglycerol [PG(38:2)-H₂O+H]⁺, m/z 785.56910 (red) in the pericarp-seed coat region. MS images were acquired in positive ion mode with 320 x 180 pixels; 5 μm pixel size; and m/z bin width: $\Delta m/z = \pm 5$ ppm. (c) Overlay of three ion images generated with high mass resolution (± 5 ppm) and low spatial resolution (50 μm pixel size) resulting in a loss of spatial information. (d) Overlay of three ion images generated with low mass resolution ($\Delta m/z = 0.1$ bin width) and high spatial resolution (5 μm) resulting in a much less distinct resolution, due to neighboring peaks of similar masses which interfere the image generation.

221x116mm (300 x 300 DPI)

1
2
3
4
5
6
7
8
9
10
11
12
13
14
15
16
17
18
19
20
21
22
23
24
25
26
27
28
29
30
31
32
33
34
35
36
37
38
39
40
41
42
43
44
45
46
47
48
49
50
51
52
53
54
55
56
57
58
59
60



182x93mm (300 x 300 DPI)

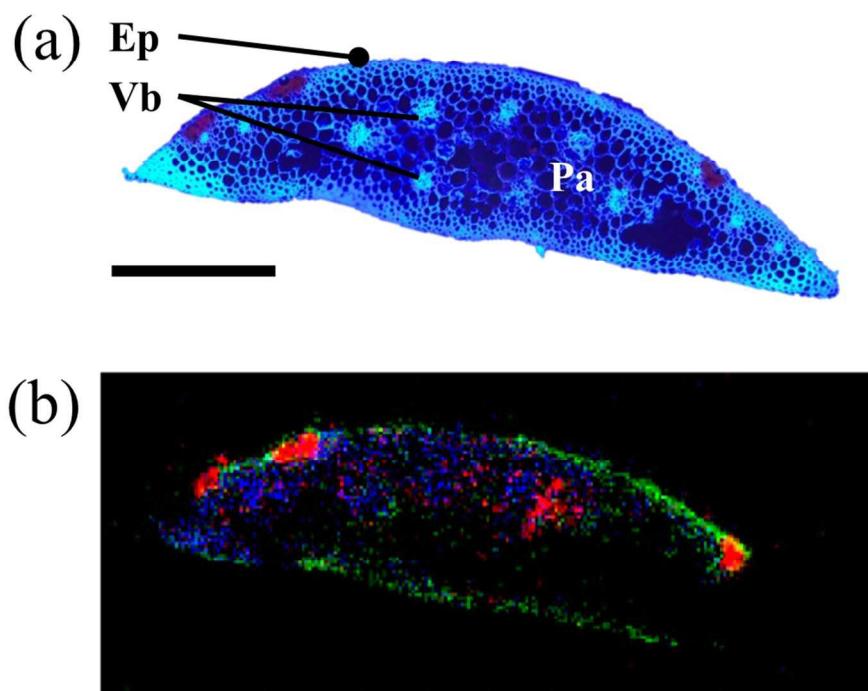


Fig. 5 Mass spectrometry imaging of a wheat rachis section at soft dough stage. (a) Optical image of a 10 μm rachis cross section taken under UV-light. The section was obtained from the center section of inflorescence and shows the epidermis (Ep) and the vascular bundles (Vb) as round inclusions within the central parenchyma cells (Pa). Scale bar 500 μm . (b) Overlay of ion images showing the tissue-specific distributions of a polyphenol glycoside $[\text{M}+\text{H}]^+$, m/z 565.15518 (green) in the epidermis; a lysophosphatidylcholine $[\text{lysoPC}(16:0)+\text{K}]^+$, m/z 534.29565 (blue) in the parenchyma; and a pheophytin $[\text{pheophytin a}+\text{K}]^+$, m/z 909.52908 (red) observed in the parenchyma and epidermis. MS images were generated with 240 x 100 pixels; 10 μm pixel size; m/z bin width: $\Delta m/z = \pm 5$ ppm. 99x79mm (300 x 300 DPI)

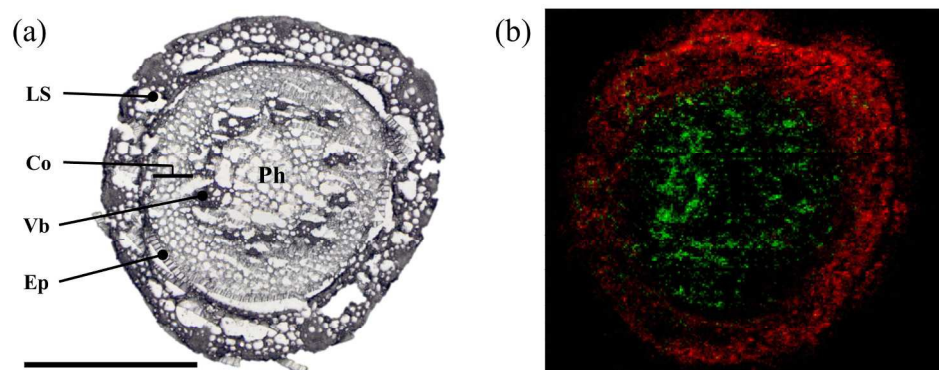


Fig. 6 MS imaging of a wheat crown at seedling stage. (a) The optical image of a 20 μm crown cross section shows the attached leaf sheath (LS) and the anatomy of seedling stem comprising the epidermis (Ep); the cortex (Co); and the pith (Ph) as central portion including the vascular bundles (Vb). Scale bar 500 μm . (b) Overlay of ion images showing the spatial distributions of a polyphenol glycoside $[\text{M}+\text{K}]^+$, m/z 565.15518 (red) the leaf sheath; and a phosphatidylcholine $[\text{PC}(36:4)+\text{K}]^+$, m/z 820.52531 (green) enriched in the vascular tissues and evenly spread within the cortex. MS images were generated with 230 x 210 pixels; 5 μm pixel size; m/z bin width: $\Delta m/z = \pm 5$ ppm.
201x87mm (300 x 300 DPI)

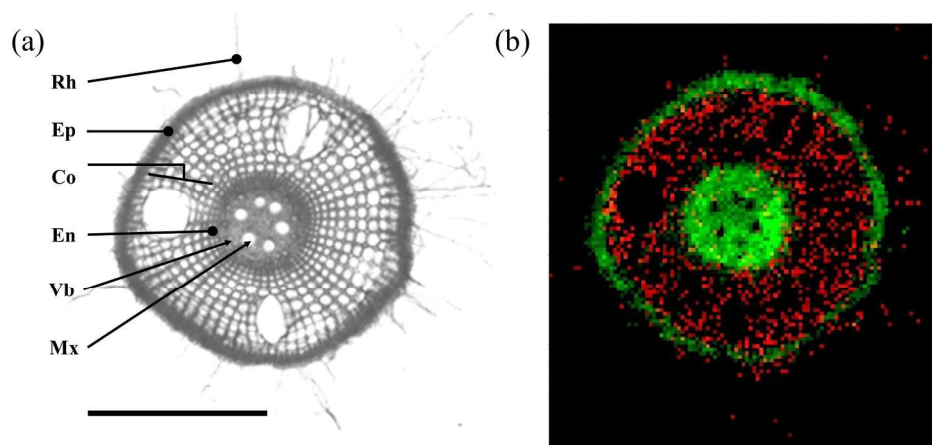


Fig. 7 Mass spectrometry imaging of a seminal rice root. (a) Optical image of a cross section of a seminal root taken from a region proximal to stem (maturation zone). The image shows the root hairs (Rh) attached to the epidermis (Ep); the central cortex (Co); the endodermis (En) which separates a central root column (stele) containing the vascular bundles (Vb) and the metaxylem vessels (Mx). The holes visible in the cortex are artefacts caused by the drying of root section in the desiccator. Scale bar 500 μm . (b) Overlay of ion images showing the spatial distributions of a [Penta-hexose+K]⁺, m/z 867.23784 (red) in the cortical layer, and a phosphatidylcholine[PC(36:4)+K]⁺, m/z 820.52531 (green) in the epidermis and the entire stele, except the metaxylem vessels. MS images were generated with 110 x 120 pixels; 10 μm pixel size; m/z bin width: $\Delta m/z = \pm 5$ ppm. 208x101mm (300 x 300 DPI)

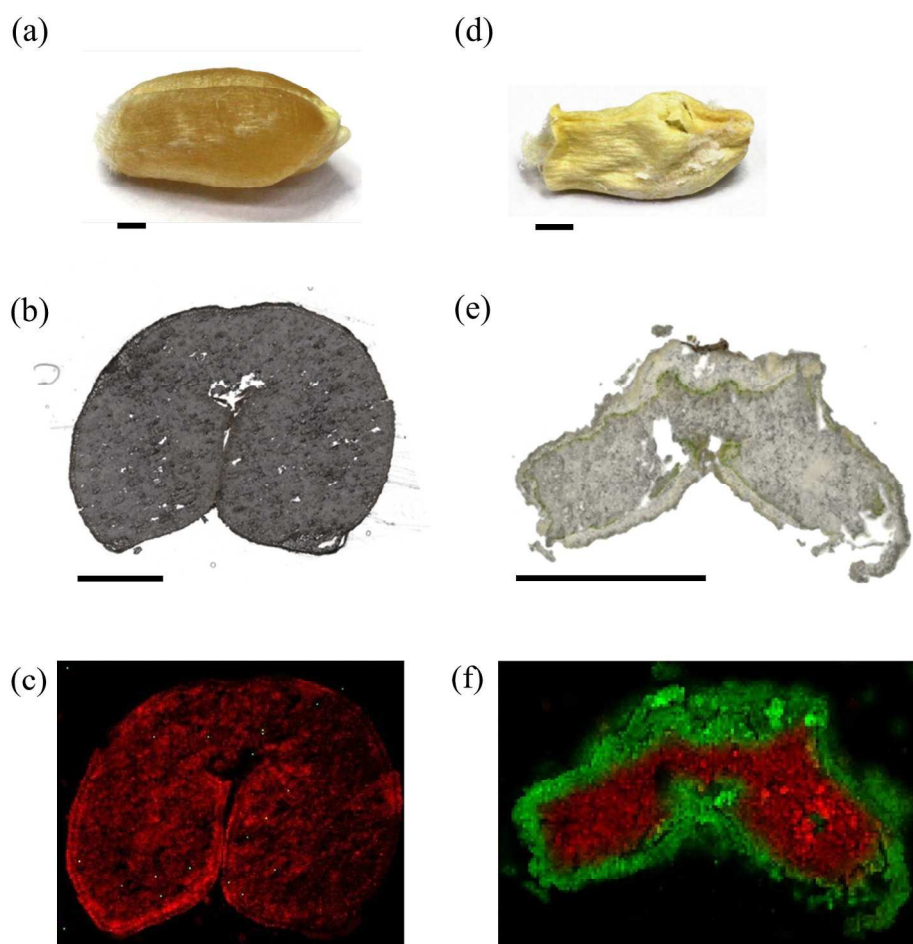


Fig. 8 Comparative Mass spectrometry imaging of uninfected and *F. graminearum*-infected wheat seeds at ripening stage. The photographic images show a healthy seed (a) and a seed infected by the fungal pathogen *F. graminearum* (d) a causal agent of the head blight disease. The seeds were sampled from the highly FHB susceptible spring wheat cv. Florence-Aurore. Scale bars 500 μm . The optical images show 20 μm transverse sections of a healthy (b) and infected seed (e), which were prepared by using the Kuwamoto method. Scale bars 500 μm . Both the photographic (d) and the optical image (e) of the infected seed demonstrate the characteristic weight reduction, shriveled and light-brown appearance associated with a highly susceptible reaction to the FHB disease. The overlay of ion images of healthy (c) and infected seed (f) show the spatial distribution of a [tetra-hexose+K]⁺ metabolite, m/z 705.18502 (red) in the entire endosperm. In contrast, the metabolite 4-(trimethylammonio)but-2-enoate [M+K]⁺, m/z 182.05779 (green) located in the entire seed bran and germ was only detected in *F. graminearum* infected seeds. MS images of healthy seed were generated with 205 x 170 pixels; 20 μm pixel size; m/z bin width: $\Delta m/z = \pm 5$ ppm. MS images of infected seed were generated with 155 x 105 pixels; 15 μm pixel size; m/z bin width: $\Delta m/z = \pm 5$ ppm.
187x185mm (300 x 300 DPI)

1
2
3
4
5
6
7
8
9
10
11
12
13
14
15
16
17
18
19
20
21
22
23
24
25
26
27
28
29
30
31
32
33
34
35
36
37
38
39
40
41
42
43
44
45
46
47
48
49
50
51
52
53
54
55
56
57
58
59
60

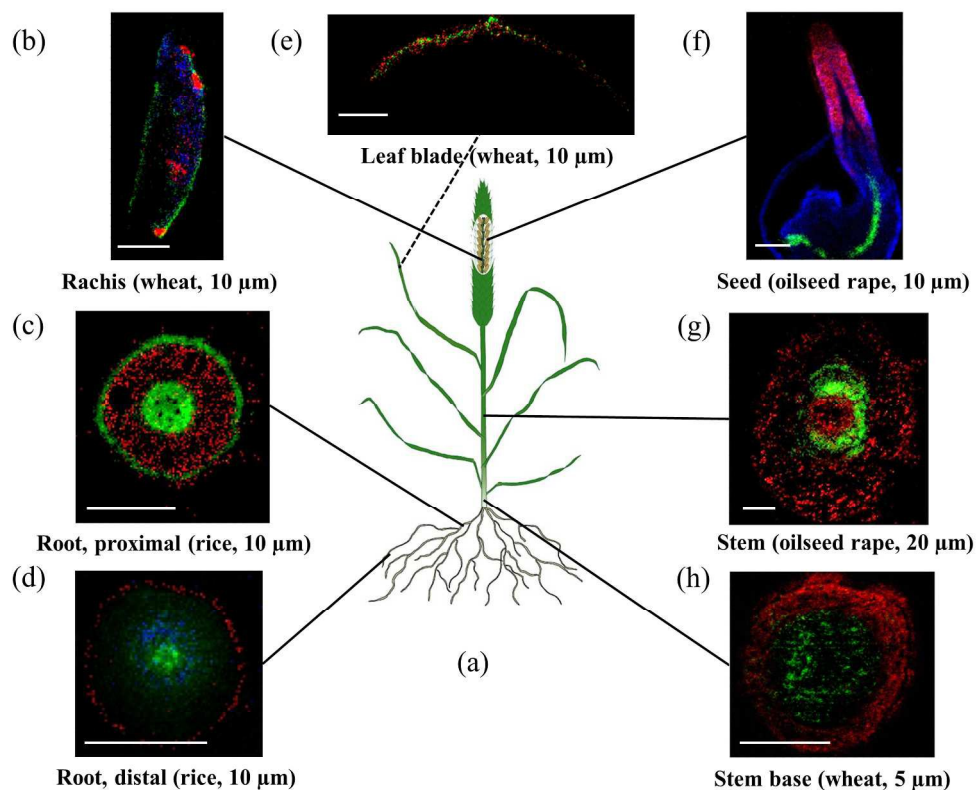


Fig. 9 Overview on the different plant structures which have been made available to high- resolution MS imaging. Scale bars in all images 500 μm . (a) Sketch of a plant. (b) MS image of wheat inflorescence rachis measured at 10 μm pixel size, details are given in Fig. 5. (c) MS image of a seminal proximal rice root (maturation zone) measured at 10 μm pixel size; details are given in Fig. 7. (d) MS image of a seminal distal rice root (elongation zone) measured at 10 μm pixel size, details are given in Supporting information, Fig. S9. (e) MS image of a wheat leaf blade measured at 10 μm pixel size, details are given in Supporting information, Fig. S12. (f) MS image of germinating oilseed rape at 10 μm pixel size, details are given in Fig. 1. (g) MS image of oilseed rape stem at 20 μm pixel size, details are given in Supporting information, Fig. S13. (h) MS image of wheat stem base at 5 μm pixel size, detail are given in Fig. 6.

217x178mm (300 x 300 DPI)